GEOPHYSICS, VOL. 63, NO. 4 (JULY-AUGUST 1998); P. 1150–1165, 21 FIGS.

3-D seismic attributes using a semblance-based coherency algorithm

Kurt J. Marfurt*, R. Lynn Kirlin‡, Steven L. Farmer*, and Michael S. Bahorich**

ABSTRACT

Seismic coherency is a measure of lateral changes in the seismic response caused by variation in structure, stratigraphy, lithology, porosity, and the presence of hydrocarbons. Unlike shaded relief maps that allow 3-D visualization of faults and channels from horizon picks, seismic coherency operates on the seismic data itself and is therefore unencumbered by interpreter or automatic picker biases.

We present a more robust, multitrace, semblance-based coherency algorithm that allows us to analyze data of lesser quality than our original three-trace cross-correlation-based algorithm. This second-generation, semblance-based coherency algorithm provides improved vertical resolution over our original zero mean crosscorrelation algorithm, resulting in reduced mixing of overlying or underlying stratigraphic features. In general, we analyze stratigraphic features using as narrow a temporal analysis window as possible, typically determined by the highest usable frequency in the input seismic data. In the limit, one may confidently apply our new semblance-based algorithm to a one-sample-thick seismic volume extracted along a conventionally picked stratigraphic horizon corresponding to a peak or trough whose amplitudes lie sufficiently above the ambient seismic noise. In contrast, near-vertical structural features, such as faults, are better enhanced when using a longer temporal analysis window corresponding to the lowest usable frequency in the input data.

The calculation of reflector dip/azimuth throughout the data volume allows us to generalize the calculation of conventional complex trace attributes (including envelope, phase, frequency, and bandwidth) to the calculation of complex reflector attributes generated by slant stacking the input data along the reflector dip within the coherency analysis window. These more robust complex reflector attribute cubes can be combined with coherency and dip/azimuth cubes using conventional geostatistical, clustering, and segmentation algorithms to provide an integrated, multiattribute analysis.

INTRODUCTION

Complex trace seismic attributes, including measures of seismic amplitude, frequency, and phase, have been used successfully in mapping seismic lithology changes for almost two decades. Multitrace relationships, including crosscorrelation techniques, have enjoyed an equally long history in the automatic picking of static corrections and, over the past decade, in the automatic picking of 3-D seismic horizons. Nevertheless, such measurements of seismic trace coherency lay buried inside a numerical algorithm. Not until Bahorich and Farmer (1995, 1996) has seismic coherency (or, perhaps more importantly, lack of coherency) been displayed and used as an attribute by itself. When there is a sufficient lateral change in acoustic impedance, the 3-D seismic coherency cube (Bahorich and Farmer, 1995, 1996) can be extremely effective in delineating seismic faults (Figures 1 and 2). This algorithm is also quite effective in highlighting subtle changes in stratigraphy, including 3-D images of meandering distributary channels, point bars, canyons, slumps, and tidal drainage patterns. Seismic coherency applied to a 3-D cube of seismic input data offers several distinct advantages over horizon dip/azimuth and shaded relief maps, including the ability to

Presented at the 65th Annual International Meeting, Society of Exploration Geophysicists. Manuscript received by the Editor October 17, 1996; revised manuscript received November 21, 1997.
*Amoco Exploration and Production Technology Group, 4502 E. 41st St. Tulsa, OK 74102-3385. E-mail: kmarfurt@amoco.com; sfarmer@amoco.com.
‡University of Victoria, 4821 Maplegrove St., Victoria, British Columbia V8Y3B9. E-mail: kirlin@engr.uvic.ca.
**Apache Corporation, 2000 Post Oak Blvd. #100, Houston, TX 77056-4400. E-mail: babo3996@a-mail.ccmail.compuserve.c.

1) accelerate the interpretation process by beginning structural and stratigraphic analysis before detailed picking begins, even on preliminary brute stack data cubes;
2) carefully analyze structural and stratigraphic features over the entire data volume, including zones that are shallower, deeper, or adjacent to the primary zone of interest;
3) identify and interpret subtle features that are not representable by picks on peaks, troughs, or zero crossings;
4) generate paleoenvironmental maps of channels and fans corresponding to sequence versus reflector boundaries; and
5) analyze features that are either internal or parallel to pickable formation tops and bottoms.

Our C_1 coherency algorithm (Bahorich and Farmer, 1995, 1996) is based on classical normalized crosscorrelation. We first define the in-line l-lag crosscorrelation, ρ_x, at time t between data traces u at positions (x_i, y_i) and (x_{i+1}, y_i) to be

$$\rho_x(t, \ell, x_i, y_i) = \frac{\sum_{\tau=-w}^{+w} u(t-\tau, x_i, y_i)u(t-\tau-\ell, x_{i+1}, y_i)}{\sqrt{\sum_{\tau=-w}^{+w} u^2(t-\tau, x_i, y_i) \sum_{\tau=-w}^{+w} u^2(t-\tau-\ell, x_{i+1}, y_i)}}, \quad (1a)$$

where $2w$ is the temporal length of the correlation window.

Next, we define the cross-line m-lag crosscorrelation, ρ_y, at time t between data traces u at (x_i, y_i) and (x_i, y_{i+1}) to be

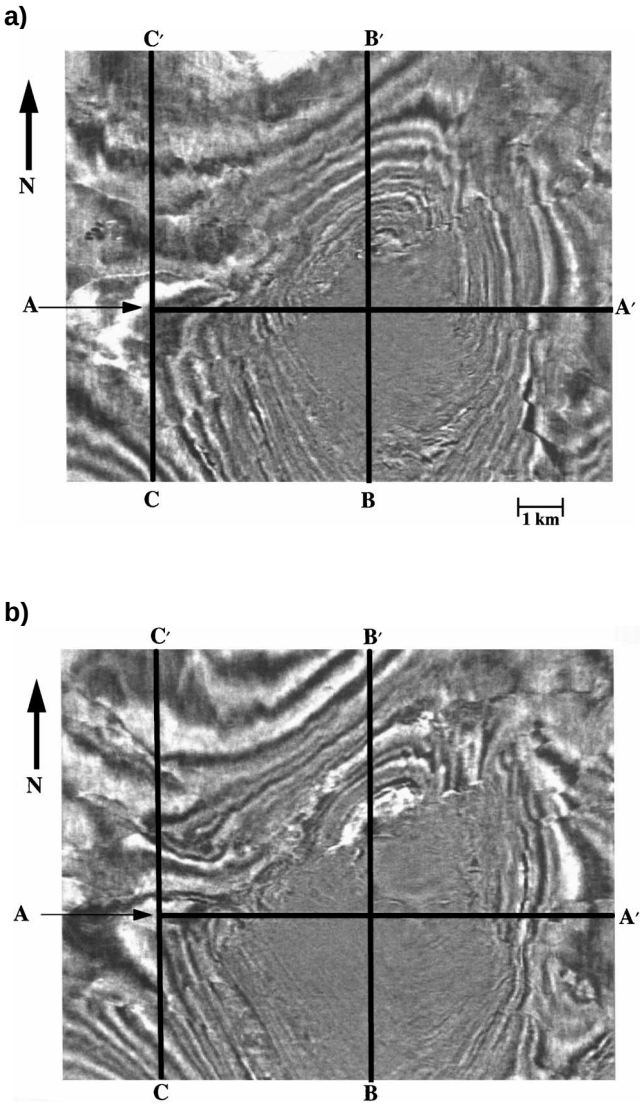

FIG. 1. Time slices through a seismic data volume at (a) $t =$ 1200 ms and (b) $t = 1600$ ms. Data courtesy of Geco-Prakla.

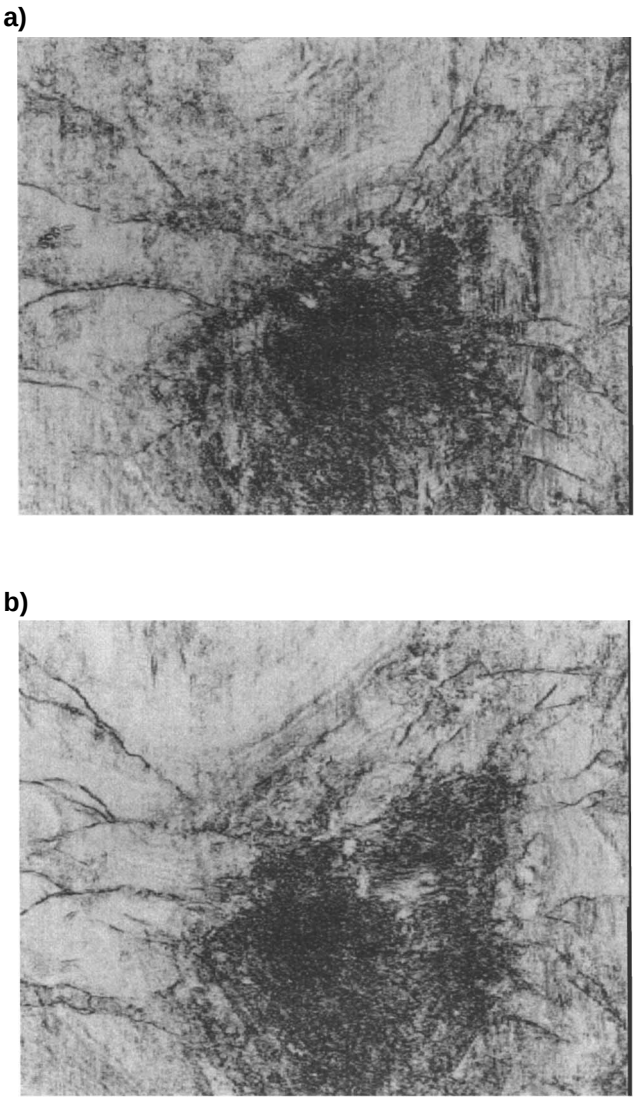

FIG. 2. Time slices through the C_1 coherency cube at (a) $t =$ 1200 ms and (b) $t = 1600$ ms, corresponding to the seismic data in Figure 1 and using the three-trace crosscorrelation algorithm given by equations (1) and (2). Temporal analysis half-window $w = 32$ ms.

$$\rho_y(t, m, x_i, y_i) = \frac{\sum_{\tau=-w}^{+w} u(t-\tau, x_i, y_i)u(t-\tau-m, x_i, y_{i+1})}{\sqrt{\sum_{\tau=-w}^{+w} u^2(t-\tau, x_i, y_i) \sum_{\tau=-w}^{+w} u^2(t-\tau-m, x_i, y_{i+1})}}. \quad (1b)$$

form the basis of both conventional and tomographic seismic velocity analysis (Taner and Koehler, 1969; Landa et al., 1993). Likewise, semblance calculations are intrinsic to robust (τ, p) analysis algorithms (Stoffa et al., 1981; Yilmaz and Taner, 1994) and f-x deconvolution algorithms.

We begin by defining an elliptical or rectangular analysis window containing J traces centered about the analysis point (Figure 4). If we center the local (x, y) axis about this analysis point, we define the semblance, $\sigma(\tau, p, q)$, to be

$$\sigma(\tau, p, q) = \frac{\left[\sum_{j=1}^{J} u(\tau - px_j - qy_j, x_j, y_j)\right]^2 + \left[\sum_{j=1}^{J} u^H(\tau - px_j - qy_j, x_i, y_j)\right]^2}{J\sum_{j=1}^{J}\left\{[u(\tau - px_j - qy_j, x_j, y_j)]^2 + \left[u^H(\tau - px_j - qy_j, x_j, y_j)\right]^2\right\}}, \quad (3)$$

These in-line (ℓ-lag) and cross-line (m-lag) correlation coefficients can then be combined to generate a 3-D estimate of coherency, ρ_{xy}:

$$\rho_{xy} = \sqrt{\left[\max_{\ell} \rho_x(t, \ell, x_i, y_i)\right]\left[\max_{m} \rho_y(t, m, x_i, y_i)\right]}, \quad (2)$$

where $\max_\ell \rho_x(t, \ell, x_i, y_i)$ and $\max_m \rho_y(t, m, x_i, y_i)$ denote those lags ℓ and m for which ρ_x and ρ_y are maximum. For high-quality data, lags ℓ and m approximately measure the apparent time dip per trace in the x- and y-directions. For data contaminated by coherent noise, estimates of apparent dip using only two traces can be quite noisy, which is a limitation of the crosscorrelation algorithm.

Crosscorrelating each trace against its neighbor for various time lags forms a different 2×2 covariance matrix for each lag pair (ℓ, m). Extending equation (1) beyond three traces requires a more general analysis of higher order covariance matrices using eigenvalue analysis (Gersztenkorn and Marfurt, 1996).

A second limitation of the three-point crosscorrelation algorithm is the assumption of zero-mean seismic signals. This is approximately true when the correlation window [$2w$ in equation (1)] exceeds the length of a seismic wavelet. For seismic data containing a 10-Hz component of energy, this requires a rather long 100-ms window that will mix stratigraphy associated with both deeper and shallower times about the zone of interest. Shortening this operator window (Figure 3) to $2w = 16$ ms results in increased artifacts attributed to the seismic wavelet. Unfortunately, a more rigorous, nonzero mean running window crosscorrelation algorithm is computationally much more expensive.

In this paper, we present our second-generation, or C_2, algorithm, which estimates coherency using a semblance analysis over an arbitrary number of traces. In addition to more robust measures of coherency, dip, and azimuth in noisy data environments, the vertical analysis window can be limited to only a few time samples, allowing us to accurately map thin, subtle, stratigraphic features.

ALGORITHM DESCRIPTION

Just as crosscorrelation forms the basis of automatic first break and reflector picking, multitrace semblance estimates

where the triple (τ, p, q) defines a local planar event at time τ, where p and q are the apparent dips in the x and y directions,

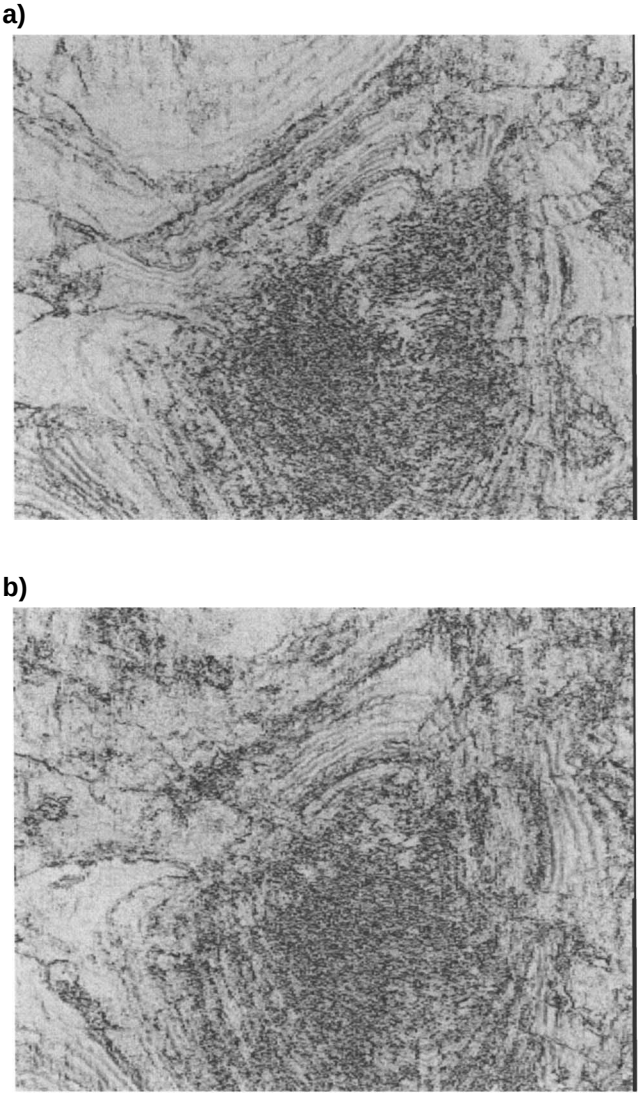

FIG. 3. Time slices through the C_1 coherency cube, corresponding to those shown in Figure 2 but with a temporal analysis half-window of $w = 8$ ms.

measured in milliseconds per meter (Figure 5), and where the superscript H denotes the Hilbert transform or quadrature component of the real seismic trace, u. Calculating the semblance of the analytic trace will allow us to obtain robust estimates of coherency even about the zero crossings of seismic reflection events. The numerator of equation (3) is the 3-D (τ, p, q) transform, $U(\tau, p, q)$, of the data $u(t, x, y)$ and is related closely to the least-squares Radon transform for 3-D dip filtering and trace interpolation:

$$U(\tau, p, q) = \sum_{j=1}^{J} u[\tau - (px_j + qy_j), x_j, y_j]. \qquad (4)$$

Indeed, we exploited such 3-D Radon transform dip filtering (Marfurt et al., 1998) to minimize the acquisition footprint because of cable feathering and dip movement artifacts as part of the data processing leading up to Figure 1. The semblance estimate given by equation (3) will be unstable for some small but coherent seismic events such as might occur if we were to sum along the zero crossings of a planar coherent event. We therefore exploit the same trick used in semblance-based velocity analysis; explicitly, we will calculate an average semblance over a vertical analysis window of height $2w$ ms or of half-height $K = w/\Delta\tau$ samples. We define this average semblance to be our coherency estimate, c:

$$c(\tau, p, q) = \frac{\sum_{k=-K}^{+K} \left\{ \left[\sum_{j=1}^{J} u(\tau + k\Delta t - px_j - qy_j, x_j, y_j) \right]^2 + \left[\sum_{j=1}^{J} u^H(\tau + k\Delta t - px_j - qy_j, x_j, y_j) \right]^2 \right\}}{J \sum_{k=-K}^{+K} \sum_{j=1}^{J} \left\{ [u(\tau + k\Delta t - px_j - qy_j, x_j, y_j)]^2 + \left[u^H(\tau + k\Delta t - px_j - qy_j, x_j, y_j) \right]^2 \right\}}, \qquad (5)$$

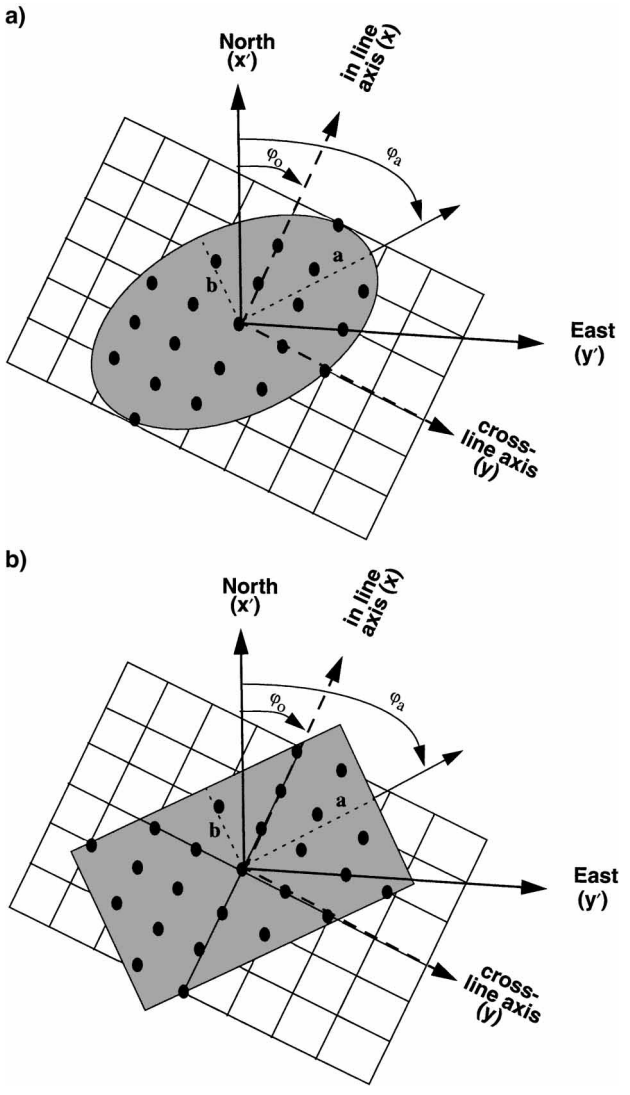

FIG. 4. (a) Elliptical and (b) rectangular analysis windows centered about an analysis point defined by length of major axis a, length of minor axis b, and azimuth of major axis ϕ_a.

where Δt is the temporal sample increment. Since our analysis window is always centered about $(x = 0, y = 0)$, the intercept time τ is identical to t.

In general, we do not know, but wish to estimate, the value of $\hat{p}, \hat{q}$ associated with the local dip and azimuth of a hypothetical planar 3-D reflection event. Horizon-based estimates of dip and azimuth have proven to be an extremely powerful interpretation tool (Dalley et al., 1989; Mondt, 1990; Rijks and Jauffred, 1991). In this paper, we will estimate (p, q) through a straightforward search over a user-defined range of discrete apparent dips. We assume the interpreter is able to estimate the maximum true dip, $d_{\max}$, measured in milliseconds per meter, from conventional in-line and cross-line seismic displays of the data (Figure 6), thereby limiting the apparent dips to

$$\sqrt{p^2 + q^2} \le +d_{\max}. \qquad (6)$$

If a and b are the half-widths of the major and minor axes of our analysis window (Figure 4), and if $f_{\max}$ is the highest temporal frequency component contained in the seismic data, then the Nyquist criterion of sampling the data at two points per period restricts the apparent dip increments, Δp and Δq, to

$$\Delta p \le \frac{1}{2a f_{\max}} \qquad (7a)$$

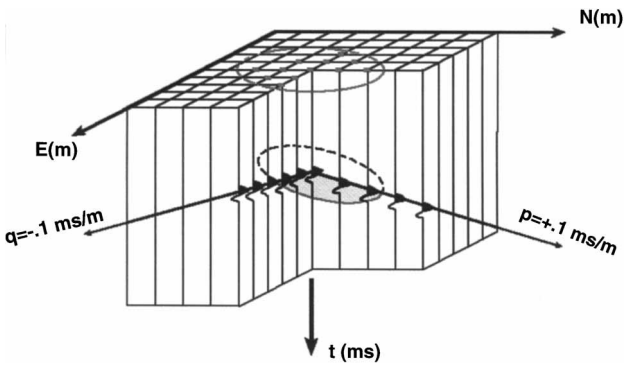

FIG. 5. Calculation of coherency over an elliptical analysis window with apparent dips $(p, q) = (0.1$ ms/m, -0.1 ms/m).

and

$$\Delta q \le \frac{1}{2bf_{\max}}. \tag{7b}$$

Our search for an estimate of the apparent dip $(\hat{p}, \hat{q})$ of the seismic reflector at time t is thus reduced to the direct calculation of $c(t, p_\ell, q_m)$ over $n_p \bullet n_q$ discrete apparent dip pairs (p_ℓ, q_m) where $n_p = 2d_{\max}/\Delta p + 1$ and $n_q = 2d_{\max}/\Delta q + 1$.

We declare the apparent dip pair (p_L, q_M) to be an estimate of the reflector apparent dips $(\hat{p}, \hat{q})$ and the coherency $c(t, p_L, q_M)$ to be an estimate of the reflector coherency, $\hat{c}$, when

$$c(t, p_L, q_M) \ge c(p_\ell, q_m) \tag{8a}$$

for all $-n_p \le \ell \le +n_p$, $-n_q \le m \le +n_q$. If necessary, we can obtain a more accurate estimate of $(\hat{p}, \hat{q})$ and $\hat{c}$ by 2-D interpolation. Here, we fit a paraboloid, $g(p, q)$, through a subset of the discrete measures of $c(t, p_\ell, q_m)$ centered about (p_L, q_M).

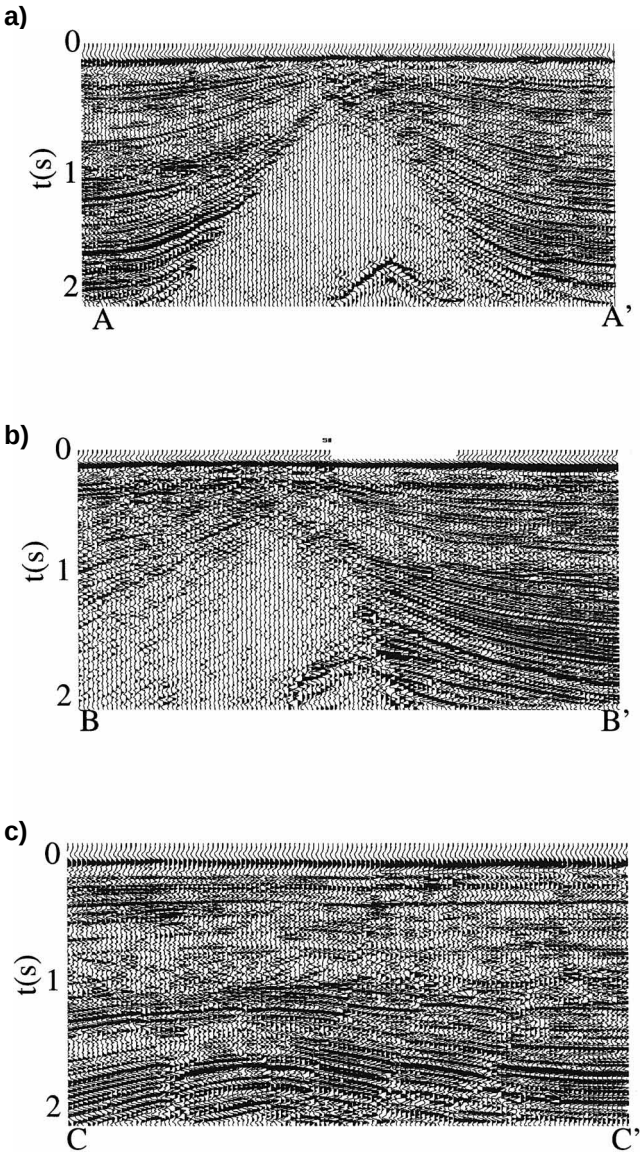

FIG. 6. Vertical slice through seismic data corresponding to lines (a) AA', (b) BB', and (c) CC', shown in Figure 1.

Then

$$\hat{c} = \max[g(p, q)] \tag{8b}$$

and $(\hat{p}, \hat{q})$ is that value of (p, q) where the maximum occurs or, mathematically,

$$(\hat{p}, \hat{q}) = g^{-1}(\hat{c}), \tag{8c}$$

where g^{-1} denotes the inverse mapping of c to (p, q).

The estimated apparent dips $(\hat{p}, \hat{q})$ are related to the estimated true dip and azimuth, $(\hat{d}, \hat{\phi})$ by the simple geometric relationships

$$\hat{p} = \hat{d} \cdot \sin(\hat{\phi}) \tag{9a}$$

and

$$\hat{q} = \hat{d} \cdot \cos(\hat{\phi}), \tag{9b}$$

where $\hat{d}$ is measured in milliseconds per meter and the angle $\hat{\phi}$ is measured clockwise from the positive x' (or north) axis. A simple coordinate rotation by angle ϕ_o is necessary when the in-line acquisition axis, x, is not aligned with the north–south, or x', axis (Figure 4).

Solid-angle discretization and display

Optimal angular discretization is important for two reasons. First, we wish to minimize the computational cost, which increases linearly with the number of angles searched. Second, at the writing of this paper, the two most popular commercial interpretive workstation software systems are limited to only 32 or 64 colors, greatly limiting the number of angles we can display. Since seismic surveys are often designed to line up with the predominant geologic strike and dip, the simplest tessellation of dip/azimuth is that along the apparent dip axes, p and q (Figure 7a). In practice, we use this tessellation only when we wish to illuminate faults cutting perpendicular to a particular strike and dip (Figure 7b).

Many geologic terranes are characterized by highly variable strike and dip; these include salt diapirs, shale diapirs, pinnacle reefs, prograding deltas, tilted fault blocks, and pop-up structures associated with wrench faulting. Even in simple geologic terranes, rarely is a single strike and dip valid over large surveys thousands of square kilometers in size.

Instead of a search over apparent dips (p, q), we could just as easily have made our search over dip and azimuth (d, ϕ). Figure 8a shows the discretization of apparent dip using equal increments Δp and Δq subject to equation (7), while Figure 8b shows the discretization using equal increments Δd and $\Delta\phi$.

Clearly, we do not wish to sample dip $d = 0$ ms/m in Figure 8b for ten different azimuths. The "Chinese checker" tessellation of Figure 8c more closely represents an equal and therefore more economic sampling of the solid angle (d, ϕ) surface with a minimum number of points. For the angular discretization shown in Figure 8c and circular analysis radius $a = b$, we choose the incremental dip Δd to be

$$\Delta d < \frac{1}{2af_{\max}}. \tag{10}$$

While it is possible to independently map coherency, dip, and azimuth, it is clear that the latter two attributes are intimately coupled. Furthermore, the confidence we have in the

dip and azimuth of a postulated reflector is proportional to the coherency. Bucher et al. (1988) have shown that the color HLS (hue, lightness, saturation) model (Foley and Van Dam, 1981) can be quite effective in displaying multicomponent seismic attributes (Figure 9). In this scheme, we first map azimuth ϕ onto the hue axis H (Figure 9b),

$$H = \phi, \tag{11}$$

where both H (commonly referred to as the color wheel) and ϕ vary cyclically between -180° and $+180^\circ$. Blue corresponds to 0°, magenta to 60°, red to 120°, yellow to 180°, green to -120°, and cyan to -60° from the north axis.

Second, we map coherency c onto the lightness axis, L (Figure 9c),

$$L = cL_{\min} + (1 - c)L_{\max}, \tag{12}$$

where $0 \le L \le 100$, $0 \le c \le 1.0$, and $L_{\min}$ and $L_{\max}$ are the minimum and maximum lightness to be used since changes in hue and saturation near $L = 0$ (black) and $L = 100$ (white) are difficult to distinguish.

Third, we map dip, d, onto the saturation axis, S (Figure 9d),

$$S = 100 \bullet \frac{d}{d_{\max}}. \tag{13}$$

We show four constant-coherency (c) surfaces through this three-component color legend in Figure 10. Note that azimuths corresponding to zero dip all appear as gray.

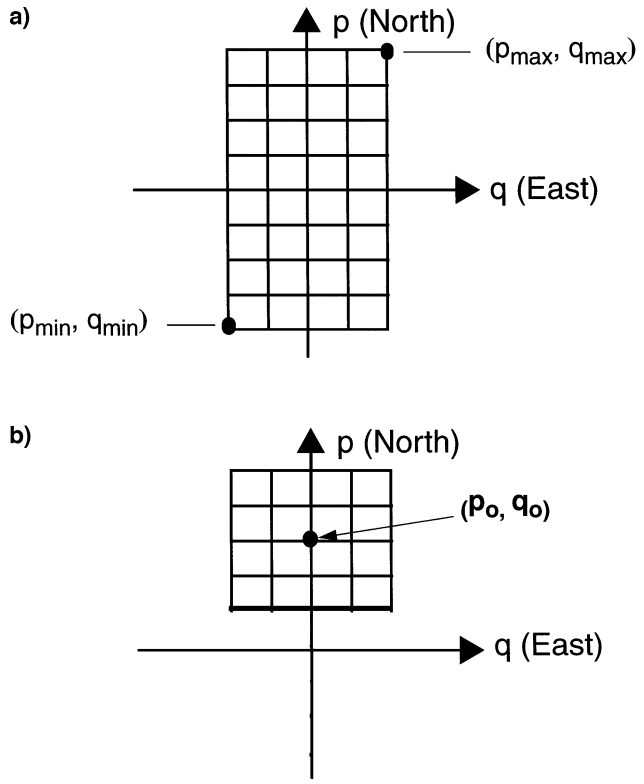

FIG. 7. Example of a rectangular dip/azimuth tessellation useful when (a) analyzing a survey having strikes and dips parallel to the acquisition axes and (b) illuminating faults cutting perpendicular to a dominant reflector strike and dip (p_o, q_o).

RESULTS

In Figure 11 we display the 3-D seismic attributes, (ϕ, c, d) corresponding to Figure 6 using our semblance-based coherency algorithm given by equations (5) and (8), and the color display technique depicted in Figures 9 and 10. These input data were temporally sampled at 4 ms and have an in-line trace spacing of $\Delta x = 12.5$ m and a cross-line trace spacing of $\Delta y = 25$ m, with the in-line acquisition oriented along the north–south axis. For this figure, we used a circular analysis window of $a = b = 30$ m (Figure 4a), thereby including a total of 11 traces in the calculation. Our maximum search dip (Figure 8c) was $d_{\max} = 0.25$ ms/m, giving rise to the 61 search angles shown in the legend displayed in Figure 10. Our temporal integration time used in equation (5) was $w = 8$ ms, or $K = 2$, thereby averaging the semblance calculation over five samples.

Lines AA' and BB' were chosen as west to east and south to north vertical slices through the center of the salt dome seen in Figure 1. South-to-north line CC' was chosen to illustrate the appearance of radial faults on a vertical slice. In Figure 11, the interior of the salt dome is represented by dark colors, corresponding to an area of generally low coherency (Figures 10c and 10d). We also notice areas of low coherency corresponding to the radial faults seen on line CC' (Figure 11c). Note that certain zones of these faults show up as coherent,

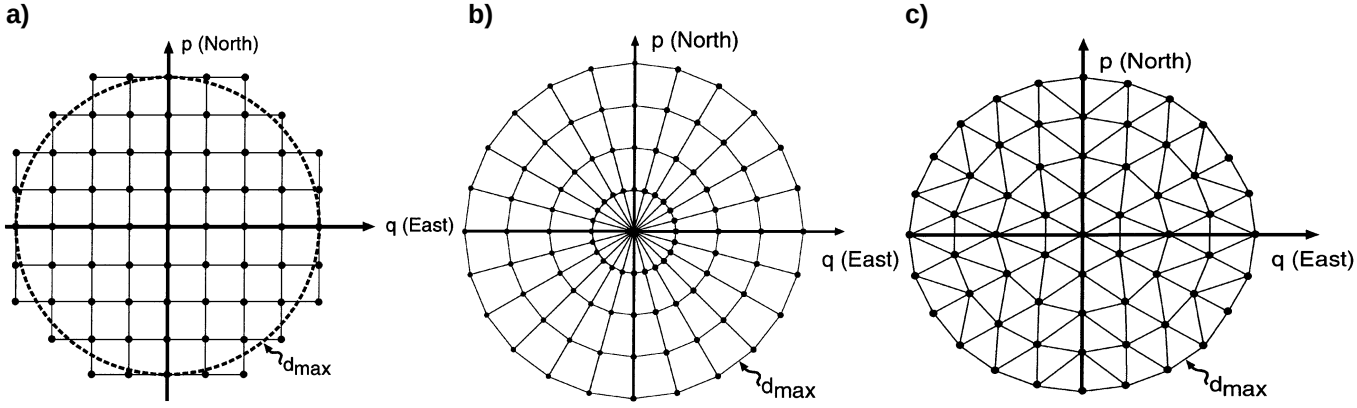

FIG. 8. Three tessellations of solid-angle dip/azimuth space: (a) a rectangular tessellation of 69 angles, (b) a radial tessellation of 97 angles, and (c) a Chinese checker tessellation of 61 angles. Each node in tessellations (a) and (c) represents an approximately equal patch of solid angle, $\Delta\Omega$.

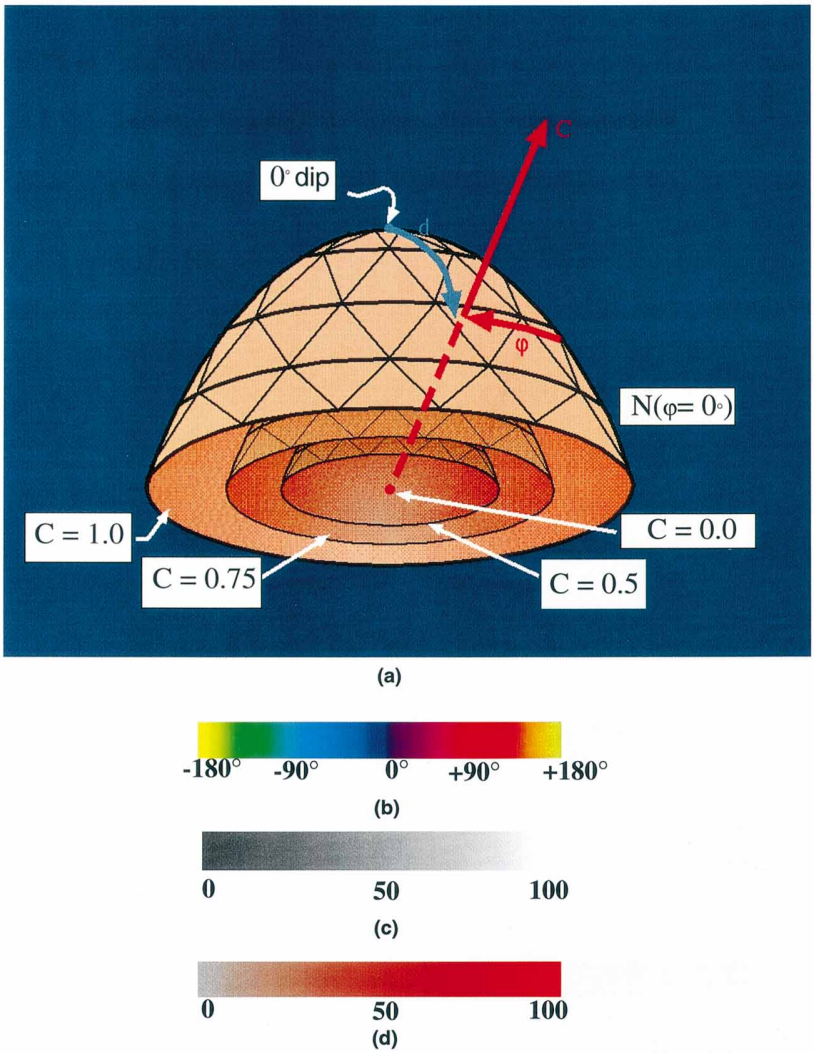

FIG. 9. (a) Mapping of 3-D seismic attributes (ϕ, c, d) to 3-D color (H, L, S) space. (b) variation of hue H with fixed values $L = 60$, $S = 100$, (c) variation of lightness L with fixed values $H = 120^\circ$ and $S = 0^\circ$, and (d) variation of saturation S with fixed values $H = 120^\circ$ and $L = 60^\circ$.

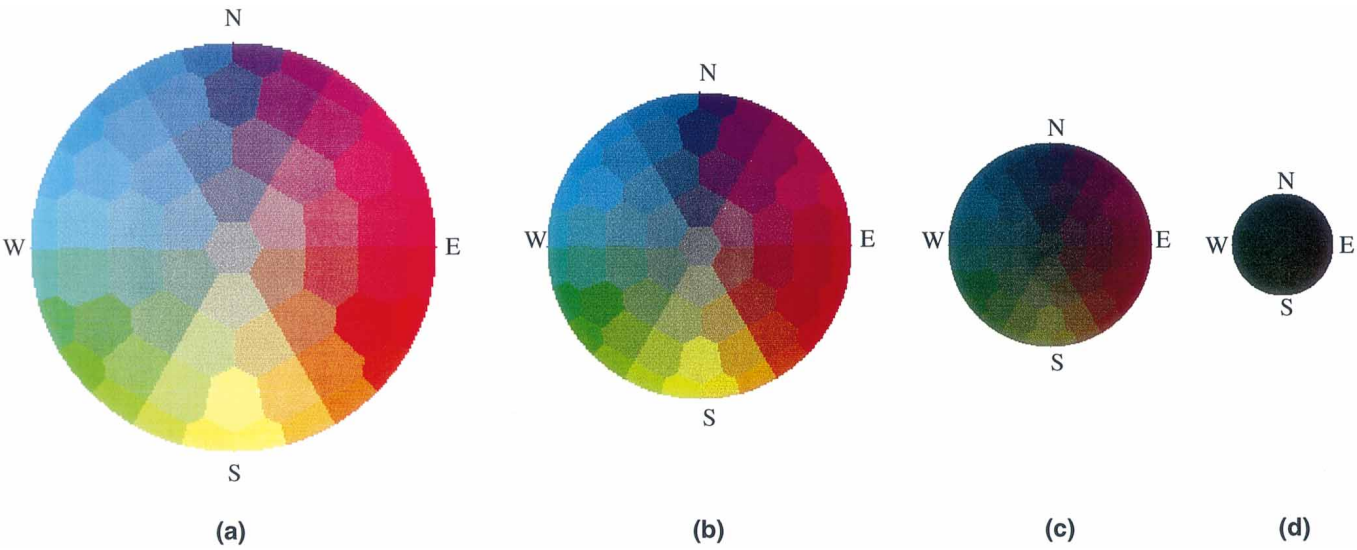

FIG. 10. Four constant-coherency, c, surfaces through the 3-D (H, L, S) color hemisphere of (ϕ, c, d) shown in Figure 9a, corresponding to (a) $c = 1.00$, (b) $c = 0.75$, (c) $c = 0.50$, and (d) $c = 0.00$.

yellow events. For the small analysis window used here, the change in dip southward across faults is indistinguishable from a locally south-dipping coherent reflector. Coherent, flat dips are represented as light gray and dominate the section away from the salt dome, in particular on most of line CC'. The blue color on the north side of the salt dome seen on north–south line BB' (Figure 11b) corresponds to sediments dipping steeply ($d = d_{\max}$) to the north. These dips become progressively shallower away from the salt dome and are thus displayed first as blue (saturation, $S = 100.0$), cadet blue ($S = 0.75$), and steel blue ($S = 0.50$) before they flatten and are displayed as gray ($S = 0.0$). The yellow on the south side of the salt dome seen on line BB' corresponds to sediments dipping steeply to the south. The salmon color on the east flank of the salt dome shown on the east–west line AA' (Figure 11a) corresponds to sediments dipping steeply to the east. These dips also become progressively shallower away from the salt dome and are displayed first as salmon ($S = 100.0$) through sienna ($S = 50.0$) and finally to gray, corresponding to flat dip. Finally, the forest green color on the west flank of the salt dome shown on line AA' corresponds to sediments dipping steeply to the west. These dips also flatten away from the salt dome and are displayed using the teal and blue-green colors shown on the west part of the color legend displayed in Figure 10. North–south line CC' is not aligned radially with the salt dome. Thus we see out-of-plane rotation of different fault blocks, with the green block indicating dips to the southwest and the magenta block indicating dips to the northeast.

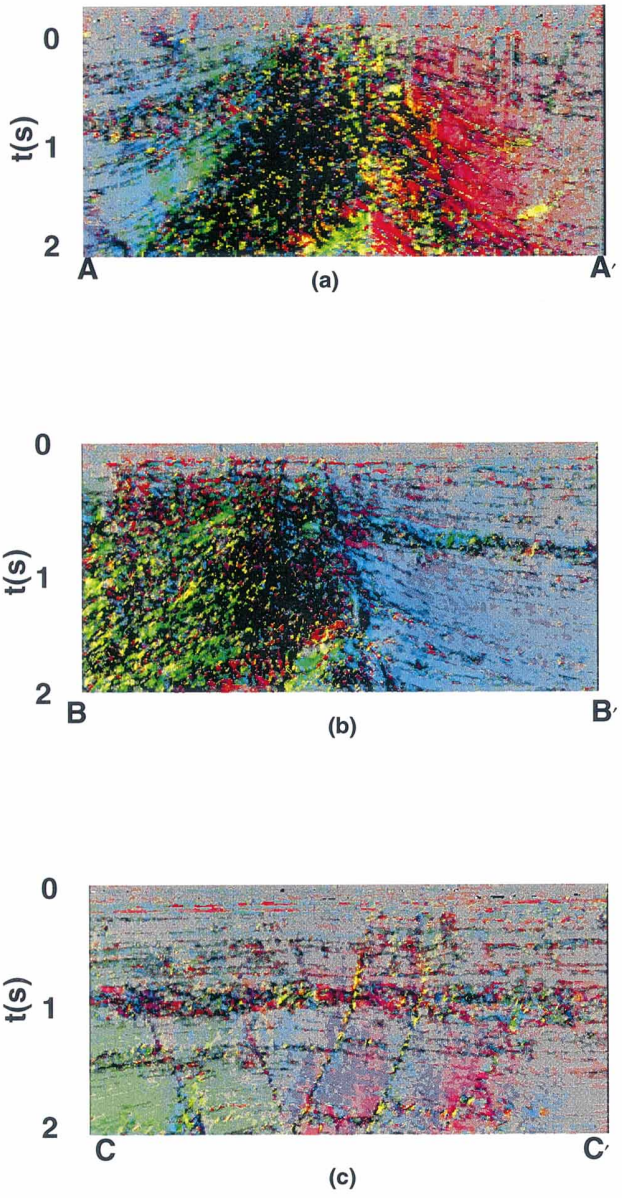

FIG. 11. The 3-D seismic attributes (ϕ, c, d) corresponding to the seismic lines displayed in Figure 6. Color legend is displayed in Figure 10.

Since these 3-D attributes were calculated for every point on the input seismic volume, we can display them as horizontal-attribute time slices (Figure 12) corresponding to the seismic time slice shown in Figure 1. Here, we see that the interior of the salt dome, as well as many portions of the radial faults, is displayed as dark colors, corresponding to incoherent zones of the data. Certain parts of the radial faults show up as abrupt local changes to bright colors and indicate the changing dip and azimuth of the reflector displacement across the fault. Because of the nearly radial symmetry of the salt diapir at $t = 1200$ ms, the dipping sediments that flank the diapir also radiate out in an azimuthally simple fashion such that their azimuths correspond quite closely to the color legend shown in Figure 10a. This pattern is somewhat less symmetric at $t = 1600$ ms, where we see shallower dips to the south than to the north. In addition, internal blocks of coherent data can be seen within the salt dome.

The color legend displayed in Figure 10 allows for only four buckets of coherency. To examine coherency c in greater detail, we plot it as a single attribute in Figure 13, applying all 184 colors to the simple grayscale shown in Figure 9c. In this display, maximum coherency, $c = 1.0$, is rendered as white, while minimum coherency, $c = 0.0$, is rendered as black. While we still see the interior of the salt diapir as a highly incoherent zone, this display better shows subtle details in the radial fault patterns. In particular, we see faults emanating from the salt dome, with some bifurcating as we move away. In addition to more continuous binning of the coherency attribute, part of this difference in perception is because the human retina sees colors and black and white using different (cone versus rod) receptors. There is also a well-documented physiological difference in the ability of men and women to differentiate between greens and blues. For this reason, many of our (often poorly dressed) male interpreters prefer the simple single-attribute coherency display shown in Figure 13 and are somewhat overawed by the multiattribute (ϕ, c, d) display shown in Figures 11 and 12. In actuality, these displays are quite complementary, with the 3-D component display highlighting conflicting dip/azimuths between adjacent rotated fault blocks and with the single component coherency display enhancing the edge, or incoherent fault discontinuity, separating them.

We also see a ringlike pattern of incoherent energy circumscribing the salt dome. To investigate the cause of this feature, we look at vertical slices through the single-component coherency cube (Figure 14) corresponding to the seismic data in Figure 6. Here, as expected, we see the interior of the salt dome as incoherent. We also recognize the incoherent submarine canyon feature described in Nissen et al. (1995) to the

north of the salt dome in Figure 14b. We notice other zones of low coherency in addition to areas of strong incoherent reflections. If one were to overlay the seismic data shown in Figure 6 with the three coherency sections shown in Figure 14, we would see a close correspondence between areas of low coherency in Figure 14 and low seismic reflection energy in Figure 6.

The ringlike features are the intersection of reflectors with the horizontal time slice. This is easily understood if we assume there is a fixed, but incoherent, level of seismic noise n throughout the data. For analysis points where the apparent dips are aligned with the peaks or troughs of strong-amplitude seismic reflectors, such that our estimate of signal energy, $s \gg n$, is high with respect to the incoherent noise, we can expect the S/N ratio to be high, giving rise to an estimate of high coherency. If, on the other hand, our analysis point is such that our apparent dips are aligned with low-amplitude seismic reflectors so the signal $s < n$ is low with respect to our incoherent noise, we can expect the S/N ratio to be low, giving rise to a low estimate of coherency. For a fixed level of noise, stratabound zones of low coherency can be geologically significant, allowing us to differentiate between low-amplitude basinal shale reflectors and higher amplitude sand/shale or carbonate reflectors on shelf margins or platforms.

Effect of vertical analysis window: structural versus stratigraphic targets

We propose two methods of increasing S/N ratio, one appropriate for structural analysis and the other appropriate for stratigraphic analysis. For the case of steeply dipping, nearly vertical faults, we can increase S/N ratio by increasing the size of our vertical integration window, w, given in equation (5). In Figure 15 we show the effect of increasing our vertical integration window from $w = 8$ ms in Figure 13b to $w = 16$ ms (Figure 15a) and $w = 32$ ms (Figure 15b). We notice two effects. First, the ringlike features seen in Figure 6 corresponding to low S/N reflectors diminish as we increase the vertical integration window size. Second, since few of our faults are truly

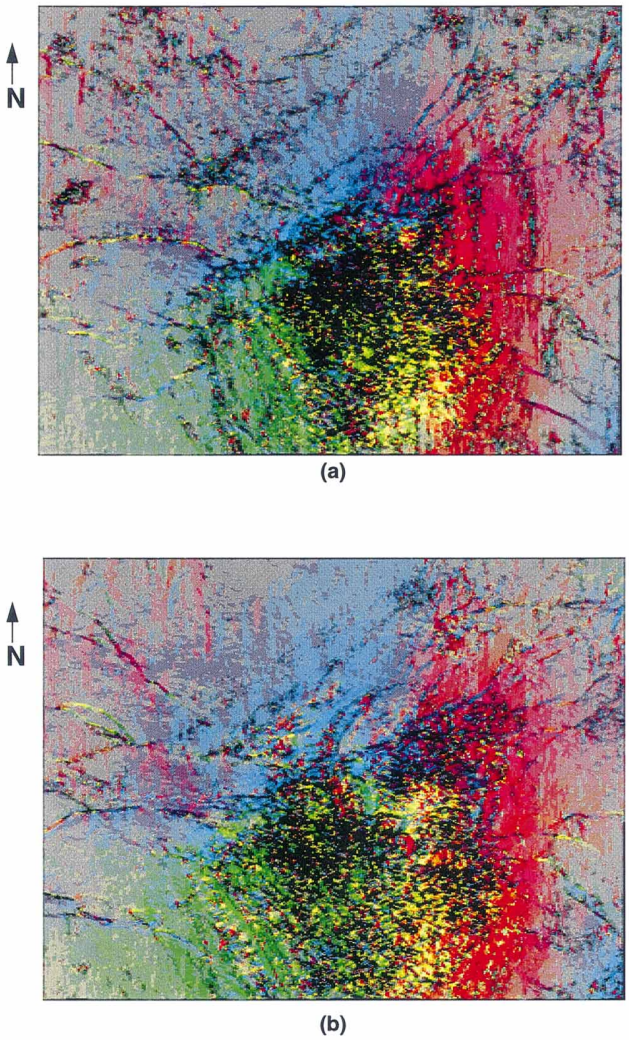

FIG. 12. Time slice through the multiattribute (ϕ, c, d) cube at (a) $t = 1200$ ms and (b) $t = 1600$ ms, corresponding to seismic data shown in Figure 1; $w = 8$ ms, $a = b = 30$ m. Color legend is displayed in Figure 10.

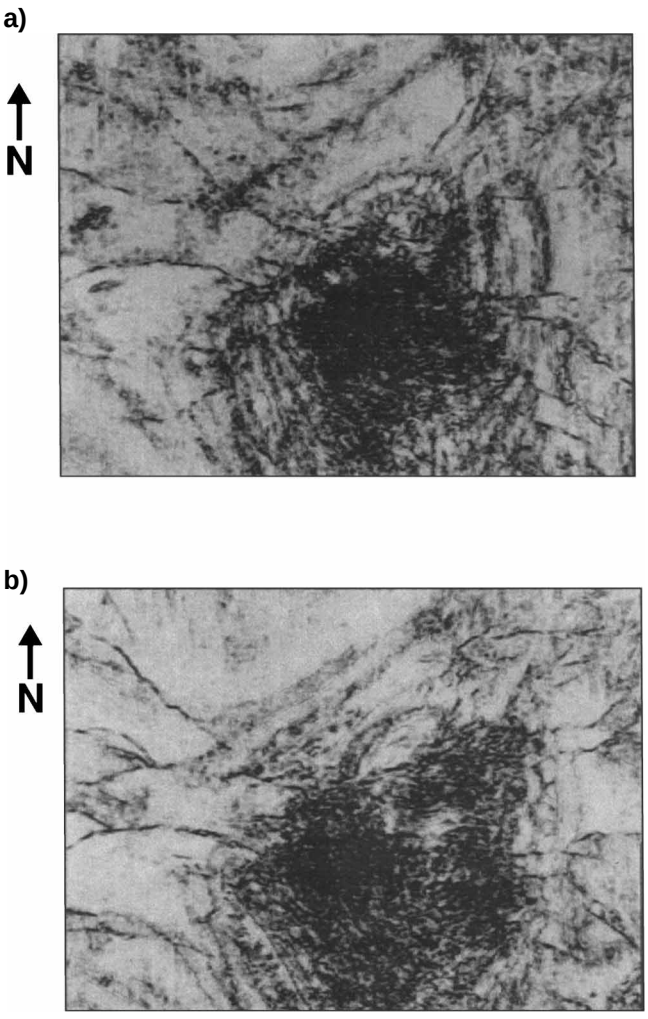

FIG. 13. Time slice through the single-coherency, c, attribute displayed using the grayscale legend displayed in Figure 9c at (a) $t = 1200$ ms and (b) $t = 1600$ ms, corresponding to seismic data in Figure 1 and multiattribute display in Figure 11; $w = 8$ ms, $a = b = 60$ m.

vertical, the lateral resolution of the faults appears to decrease as we increase the vertical window size. The analysis window of $w = 16$ ms (Figure 15a), which would encompass a full cycle of the peak 30-Hz energy in our data, appears to be a good compromise.

The second method of increasing S/N ratio, equally appropriate for stratigraphic and structural analysis, is to extract our coherency generated for the entire seismic data cube along an interpreted stratigraphic horizon. It is much more likely that a single reflection event will have less variability in S/N ratio than a horizontal time slice. In general, extracting coherency data corresponding to a zero crossing would greatly exacerbate the effect of seismic noise on our coherency display. Fortunately, most automatic picker software tracks the extremum peak or trough of a seismic event, thus maximizing S/N ratio. In practice, we analyze coherency along a stratigraphic horizon by first flattening the data along the horizon of interest and then calculating (ϕ, c, d) within a window of height $2w$. This approach is somewhat more sensitive to busts in automatic (and human) pickers than the alternative of calculating a cube of coherency and then extracting the results because cycle skip glitches in the picking will misalign the seismic wavelet and therefore almost always appear incoherent. Figure 16 shows an

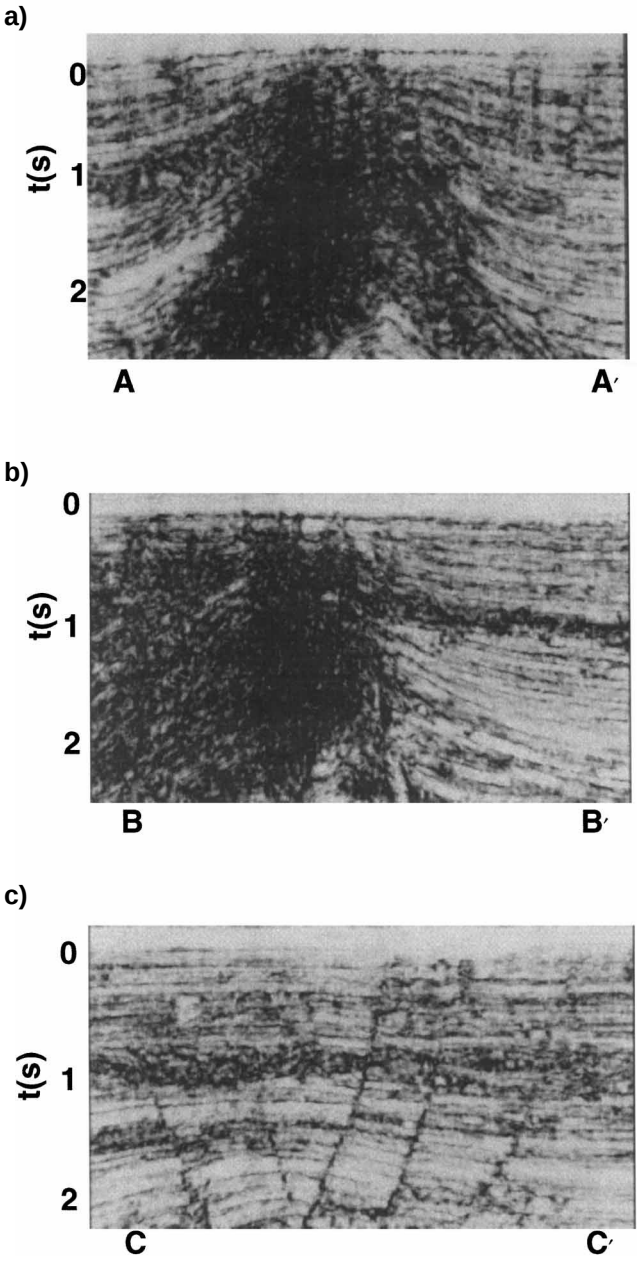

FIG. 14. Coherency, c, estimated using equations (5) and (8), corresponding to seismic data and dip/azimuth shown in Figures 6 and 11. Vertical integration window $w = 8$ ms. Color legend is given in Figure 9c, black corresponds to $c = 0.0$, white to $c = 1.0$. Note low coherency submarine canyon feature at 1 s described by Nissen et al. (1995).

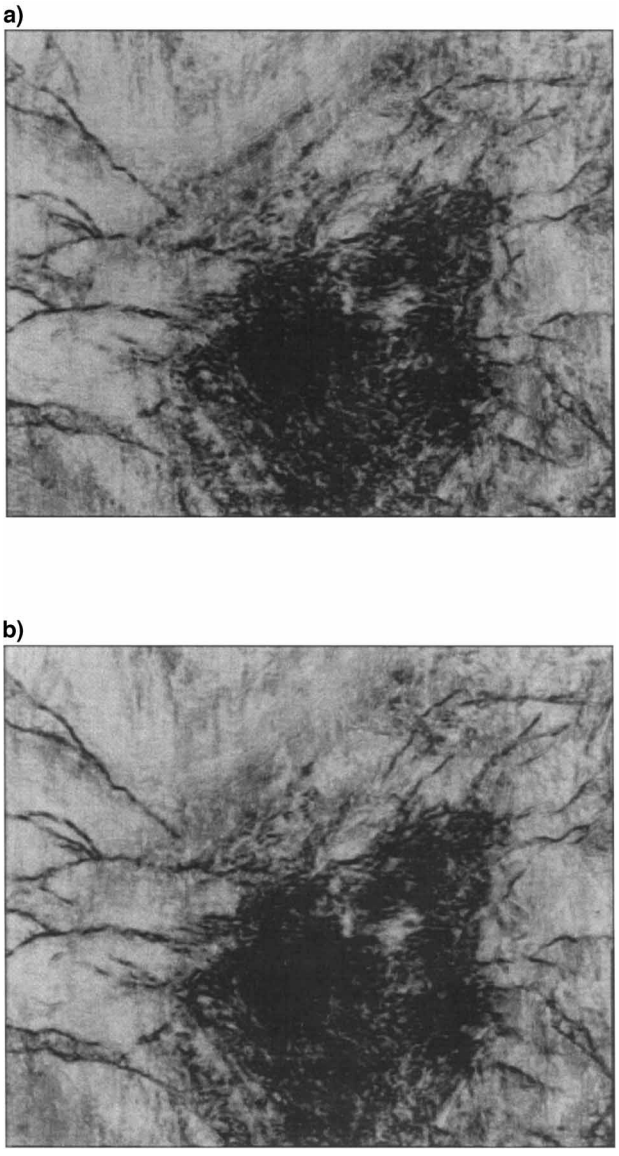

FIG. 15. Sensitivity of coherency images of structural features generated using equation (5) to vertical window length w for a fixed eleven-trace $a = b = 30$ m analysis window. (a) $w = 16$ ms; (b) $w = 32$ ms. Compare to Figure 13b, where $w = 8$ ms.

amplitude extraction corresponding to a picked trough along the Pleistocene horizon for the survey shown in Figure 1. The salt dome discussed earlier lies in the southwest corner of this survey. Data quality is excellent, and a great many details of a Pleistocene-age Mississippi distributary channel system can be seen easily. We perform the same $a = b = 30$ m, 11-trace semblance-based coherency analysis as we did for the structural (salt dome) analysis for vertical integration windows of $w = 4$ ms, $w = 8$ ms, and $w = 32$ ms and display the results in Figures 17a, b, and c, respectively.

The first thing we note are multiple east–west and north–south linear artifacts corresponding to busts in our autopicking. A major east–west fault, FF', shows up well for all three parameter choices but is laterally better resolved, with small en echelon faulting visible, for the shortest analysis window (Figure 17a). Fault ff', having significant structural throw, is rendered as an area of significant busts in our picking. Laterally narrow and presumably shallow, channels gg' and hh' show up sharply for the smallest vertical analysis window of $w = 4$ ms. Likewise, the (presumably shallow) tidal channel features corresponding to reworked deltaic sands, H, described in Haskell et al. (1995) are also most pronounced when using a short vertical analysis window. Since these shallow features do not persist for any distance above or below the interpreted stratigraphic horizon, the inclusion of any data from above or below this horizon adds uncorrelated amplitude variations, thereby making these discontinuities look more coherent and washed out (Figure 17c). If the time samples above or below the interpreted horizon contain independent, perhaps strong amplitude discontinuities, these discontinuities will bleed into our analysis for large vertical windows, giving a stratigraphic horizon containing features mixed from stratigraphically different horizons generated at different geologic times. The additional channel features jj' and kk' seen in Figure 17c conflict with the generally self-consistent distributary channel feature seen in Figure 17a and, through analysis of neighboring horizon slices, can be seen to be leakage of stratigraphic features corresponding to units (having a different distributary pattern) above and below the picked horizon.

Effect of horizontal analysis window: lateral resolution versus S/N ratio

Having analyzed the effect of varying our vertical analysis window, we now turn to analyzing the effect of increasing our horizontal analysis window. By examination of equation (5), it is clear that the computational cost of our analysis increases linearly with the number of traces included in our analysis. However, comparing our semblance-based eleven-trace coherency time slice of Figure 15b with those of our original three-trace crosscorrelation coherency time slice in Figure 2b, each having an identical vertical analysis window of $w = 32$ ms, we are led to believe that adding more traces to the computation can increase our S/N ratio. We therefore analyze the effect of running the minimal ($a = 12.5$ m and $b = 25$ m, or five-trace) elliptical analysis window (Figure 18a) and increasing our analysis window to $a = b = 55$ m, or 29 traces (Figure 18b) and compare the results to our eleven-trace ($a = b = 30$ m) analysis window shown in Figure 15b. In general, the S/N ratio increases as we increase the size of the analysis window. The lateral resolution decreases simply because more large-aperture than small-aperture analysis windows encompass a given discrete discontinuity.

In Figure 19, we examine our estimate of multiattribute (ϕ, c, d) time slices corresponding to the five-trace and 29-trace analysis window coherency time slices shown in Figure 18. The

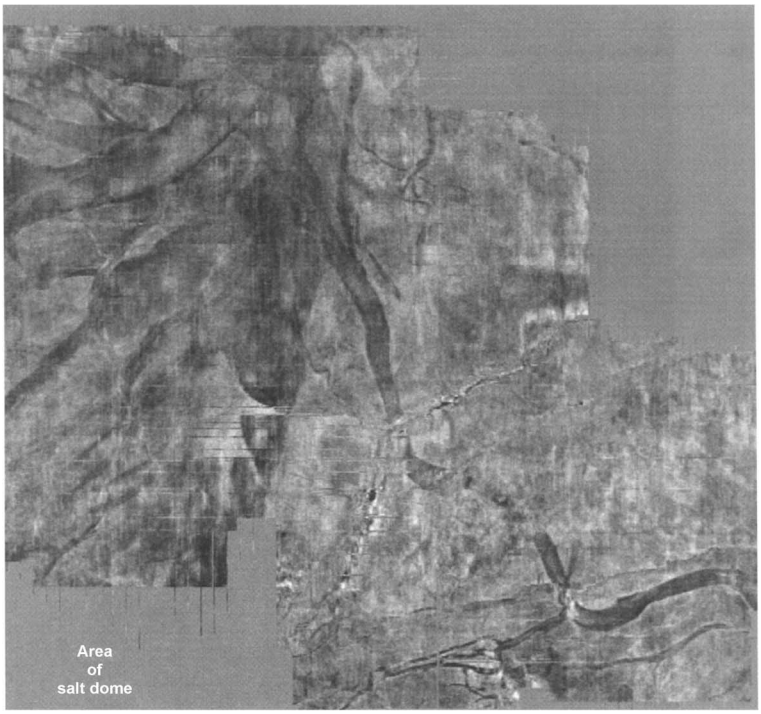

FIG. 16. Seismic data exacted along an interpreted Pleistocene horizon showing the Paleo-Mississippi distributary channels. Data courtesy of Geco-Prakla.

stability of our dip/azimuth estimates increases with the number of traces in the calculation. The analysis window can be increased (at greater computational cost) until it becomes so large that the reflector curvature is no longer well approximated by a plane.

ESTIMATION OF REFLECTOR-BASED COMPLEX TRACE ATTRIBUTES

Once we have estimated the dip/azimuth of a postulated reflector, it is possible to obtain a smoother and more robust multitrace estimate of the conventional complex trace attributes (Taner et al., 1979). A general description of the use of seismic attribute maps can be found in Bahorich and Bridges (1992) and Rijks and Jauffred (1991). Instead of calculating these attributes on a single trace, we calculate the attributes of the angle stack of traces falling within the analysis window corresponding to the extended reflector dip. That is, we calculate

$$a_i(\tau, p, q) = \{[U(\tau, p, q)]^2 + [U^H(\tau, p, q)]^2\}^{1/2}, \quad (14a)$$

$$\psi_i(\tau, p, q) = \tan^{-1}[U^H(\tau, p, q)/U(\tau, p, q)], \quad (14b)$$

$$f_i(\tau, p, q) = \frac{\left[U(\tau, p, q)\dfrac{\partial U^H}{\partial \tau}(\tau, p, q) - U^H(\tau, p, q)\dfrac{\partial U}{\partial \tau}(\tau, p, q)\right]}{[U(\tau, p, q)]^2 + [U^H(\tau, p, q)]^2}, \quad (14c)$$

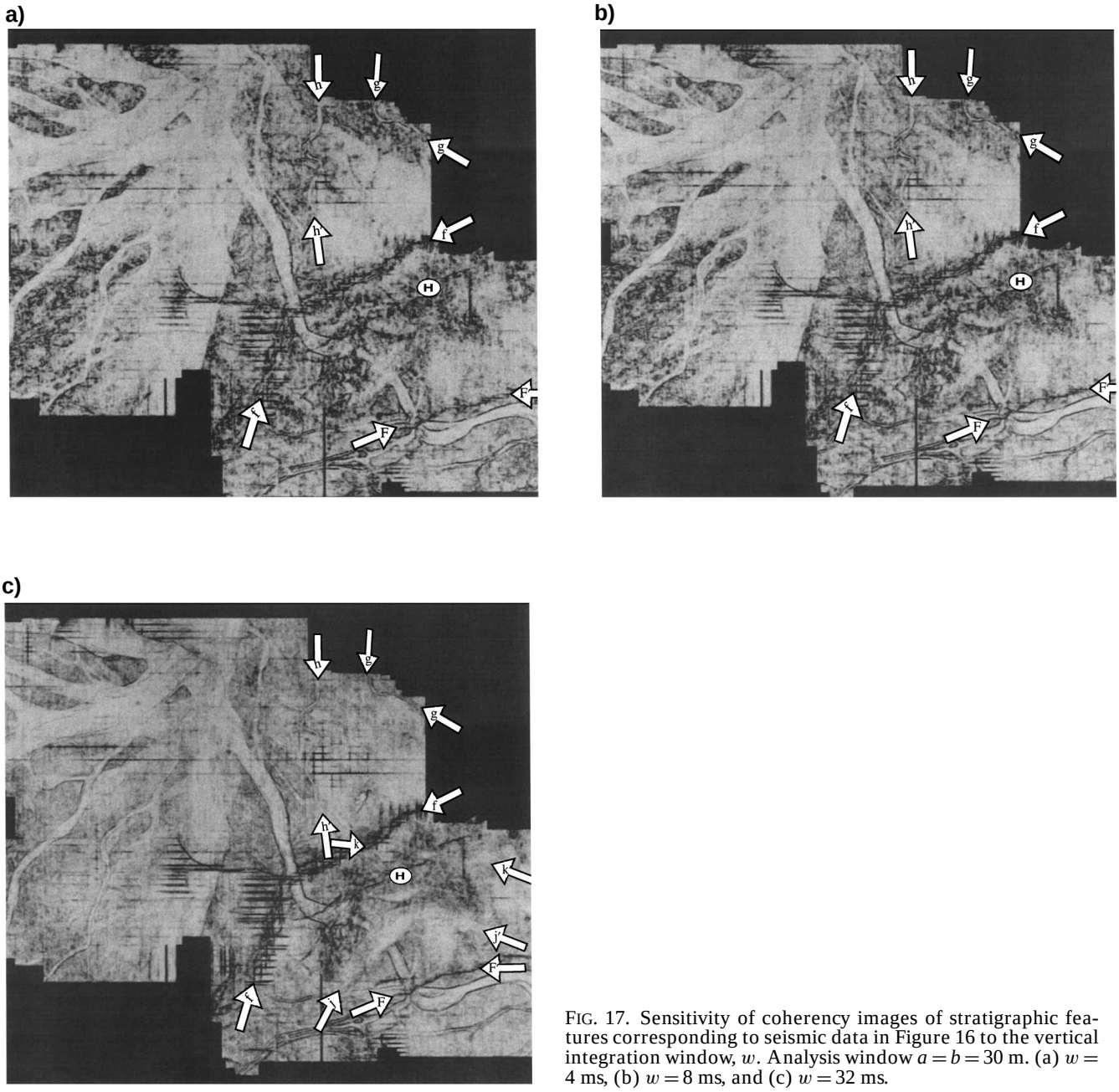

FIG. 17. Sensitivity of coherency images of stratigraphic features corresponding to seismic data in Figure 16 to the vertical integration window, w. Analysis window $a = b = 30$ m. (a) $w =$ 4 ms, (b) $w = 8$ ms, and (c) $w = 32$ ms.

and

$$b_i(\tau, p, q) = \frac{\left| U(\tau, p, q)\frac{\partial U}{\partial \tau}(\tau, p, q) + U^H(\tau, p, q)\frac{\partial U^H}{\partial \tau}(\tau, p, q) \right|}{[U(\tau, p, q)]^2 + [U^H(\tau, p, q)]^2}, \quad (14d)$$

where $a_i(\tau, p, q)$ is the envelope, or instantaneous amplitude; $\psi_i(\tau, p, q)$ is the instantaneous phase; $f_i(\tau, p, q)$ is the instantaneous frequency; $b_i(\tau, p, q)$ is the instantaneous bandwidth (Cohen, 1993); $U(\tau, p, q)$ is the (τ, p, q) transform of the input data given by equation (4); and $U^H(\tau, p, q)$ denotes the Hilbert transform, or quadrature of $U(\tau, p, q)$.

In addition to these instantaneous attributes, additional attributes characterize the signal within a given lobe of the trace envelope as the attribute at the peak of the envelope at time τ_e. These include (Bodine, 1984) the response envelope,

$$a_r(\tau, p, q) = a_i(\tau_e, p, q); \quad (15a)$$

the response phase,

$$\psi_r(\tau, p, q) = \psi_i(\tau_e, p, q); \quad (15b)$$

the response frequency,

$$f_r(\tau, p, q) = f_i(\tau_e, p, q); \quad (15c)$$

and the response bandwidth,

$$b_r(\tau, p, q) = b_i(\tau_e, p, q). \quad (15d)$$

By slant stacking the input data along the true dip direction, the slowly varying amplitude, phase, frequency, and bandwidth components of the reflector will be enhanced.

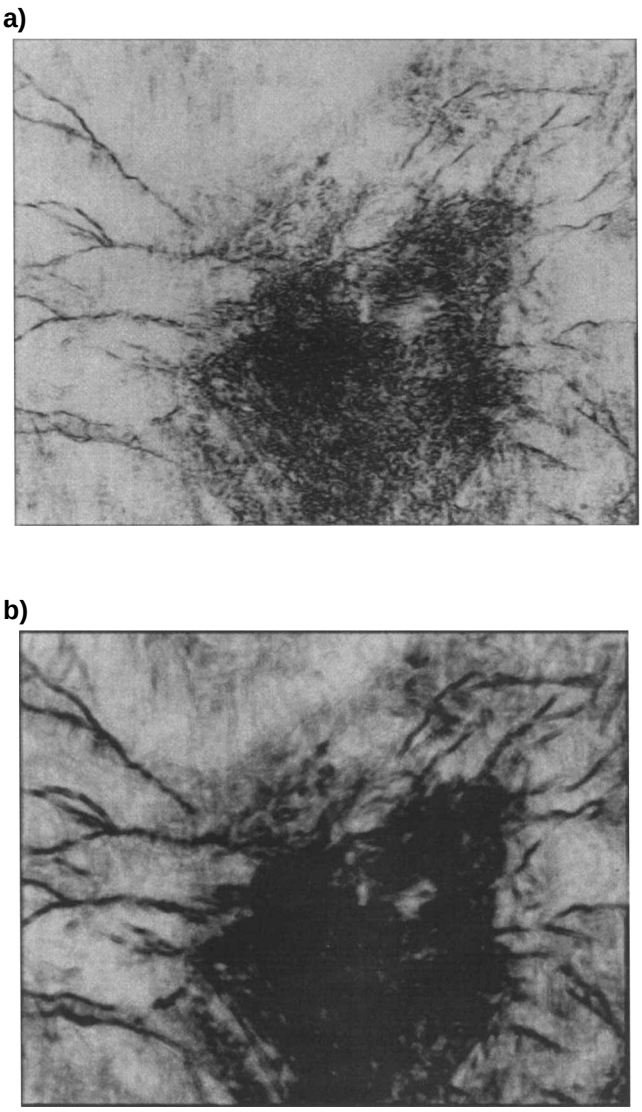

FIG. 18. Sensitivity of lateral resolution to size of the analysis window shown in Figure 4a. Coherency, c, for (a) a five-trace analysis window with $a = 12.5$ m and $b = 25$ m and (b) a 29-trace analysis window with $a = b = 55$ m. Compare to the eleven-trace calculation of Figure 15b, where $a = b = 30$ m.

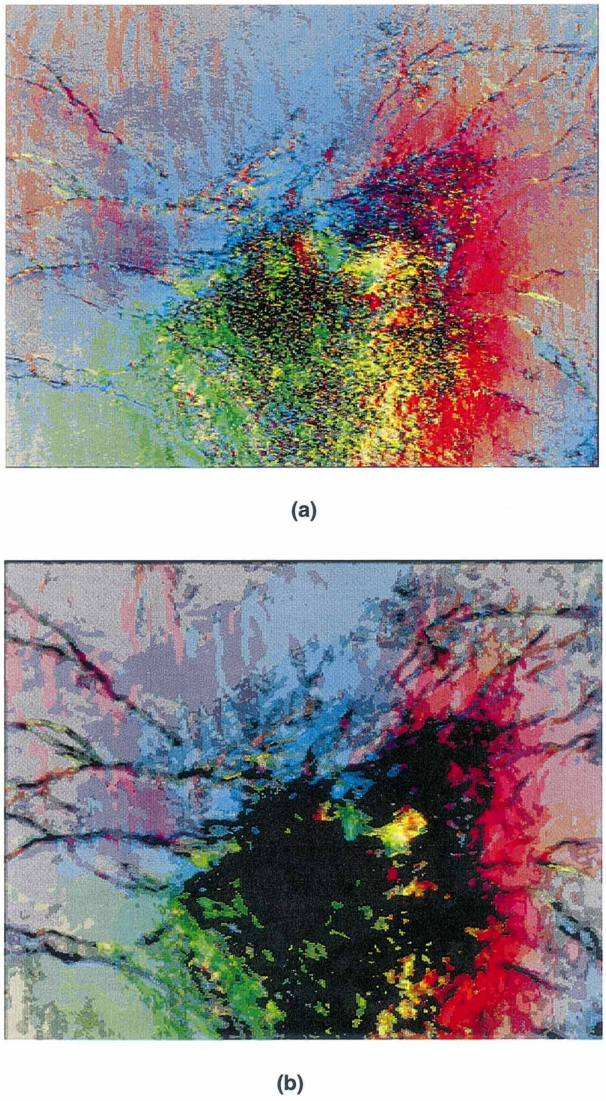

FIG. 19. Time slice through the multiattribute (ϕ, c, d) cube at 1600 ms; $w = 16$ ms. (a) Five-trace analysis window; $a = 12.5$ m, $b = 25$ m. (b) Twenty-nine-trace analysis window, $a = b = 55$ m. Color legend is displayed in Figure 10.

Figure 20 shows the conventional single-trace response frequency corresponding to the interpreted horizon slice shown in Figure 16. Figure 21 shows the same response frequency attribute f_r but calculated from $U(\tau, \hat{p}, \hat{q})$, where $(\hat{p}, \hat{q})$ are coherency-based estimates of the apparent dip of the reflector. We represent areas of low coherency values, $c < 0.5$, by shades of gray, graphically indicating the decreased probability of there being a planar reflector.

The response frequency is a numerical estimate of the amplitude-weighted average frequency of the reflector wavelet spectrum. For this reason it is centered about the source wavelet center frequency of 30 Hz. In Figure 20 we note that the response frequency is generally lower in the channels, indicated by yellow and blue, while the shale matrix is represented by red. The spectrum of the overlying channel jj', as discussed in Figure 17c, is particularly low. In general, the spectrum of wider, temporally thicker channels is tuned toward lower frequencies. The reflector response frequency given by equation (15c) is displayed in Figure 21. Even though each analysis trace is averaged over only the five-point spatial analysis window, along the dip/azimuth direction the resulting image has considerably less snow than Figure 20. In particular, the narrow channel hh' is much better resolved in Figure 21 than in Figure 20.

CONCLUSIONS

Our second-generation (or C_2) algorithm, based on 3-D semblance calculations, provides an excellent measurement of seismic coherency. By using an arbitrary-size analysis window, we are able to balance the conflicting requirements between maximizing lateral resolution and increasing S/N ratio that is not possible when using our original (C_1) or three-trace crosscorrelation algorithm. In the C_2 algorithm, we obtain accurate measurements of coherency using a short vertical integration window on the order of the shortest period in the data, whereas the zero mean crosscorrelation C_1 algorithm requires an integration window greater than the longest period in the data. Thus, our semblance algorithm results in less vertical smearing of geology than our original crosscorrelation algorithm, even for large spatial analysis windows—of particular importance in mapping stratigraphic features. The quality of seismic coherency images is directly related to the quality of the input seismic data. Coherency renders carefully migrated faults as sharp discontinuities, while undermigrated fault edge diffractions appear to be crossing but relatively coherent events. Likewise, backscattered seismic noise cutting across otherwise coherent reflectors results in an overall diminished coherency. In addition to robust measures of coherency, we also are able to

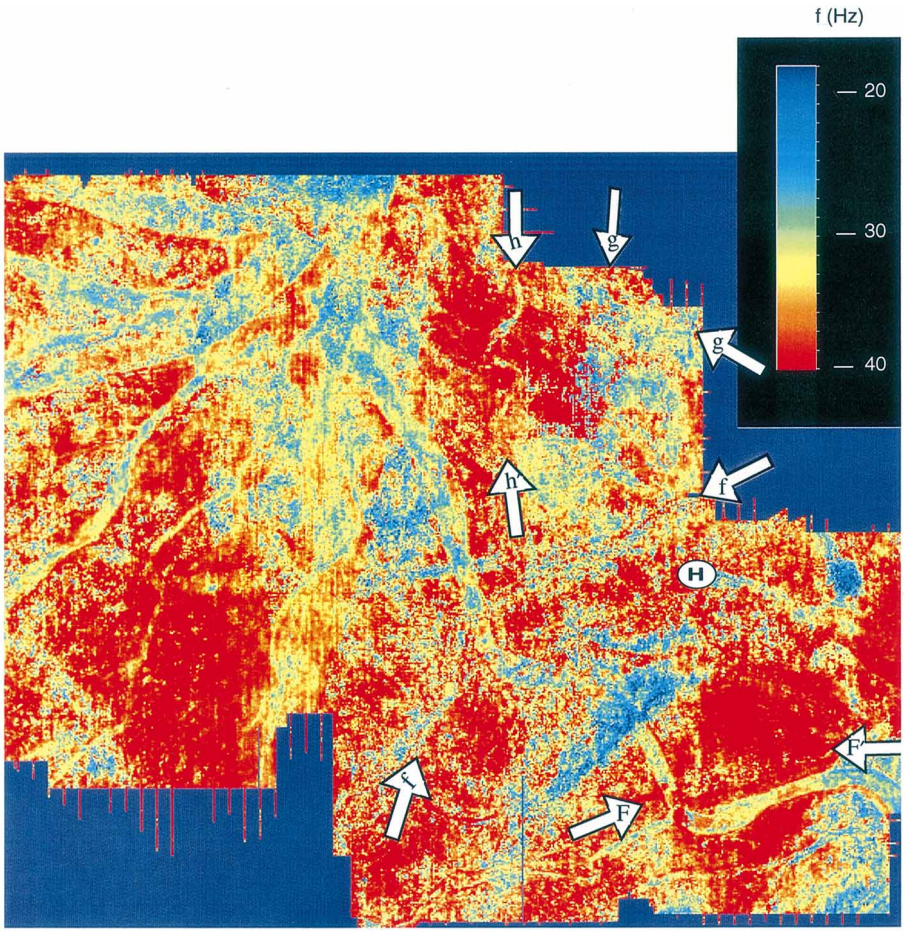

FIG. 20. Trace response frequency described by Bodine (1984) generated using equation (15c), corresponding to the seismic data shown in Figure 17.

generate robust estimates of reflector dip/azimuth throughout the entire data volume. As one would anticipate, increasing the number of traces included in our coherency analysis window increases angular resolution, decreases lateral resolution, and increases the computational cost.

Equally important to the coherence estimate, the C_2 or semblance algorithm affords us a direct means of estimating the 3-D dip/azimuth of each reflector event in the data cube. In some cases these dip/azimuths may be related to conventional time-structure maps defining formation boundaries. In other cases, such as when flattening along an interpreted horizon, they may be used in accelerating the mapping onlap, offlap, and concordancy. Changes in dip/azimuth are indicative of folding, scouring, mass wasting, fault-block rotation, and/or downdropping of adjacent fault blocks. When extracted relative to a sequence boundary, dip/azimuth maps can be used in the analysis of progradation, fan, and levee complexes. Like coherency (by either the crosscorrelation or semblance algorithm), estimation of the dip/azimuth cube can be achieved prior to any interpretation of the data for use in a gross overview of the geologic setting. In this reconnaissance mode, the coherency and dip/azimuth cubes allow us to pick key dip and strike lines crossing important structural or sedimentologic features very early in the interpretation phase of a project. In the interpretation mode, we relate these dip/azimuths to formation and/or sequence boundaries, such that we will be able to map progradation and transgression patterns of the internal structure in three dimensions.

Finally, having estimated the dip/azimuth at every point in our data cube, we are able to apply our conventional seismic trace attributes to reflector wavelet envelope, phase, frequency, and bandwidth to locally planar reflectors, thereby significantly increasing our S/N ratio. The authors believe that these enhanced complex trace attributes can be combined with coherency and dip/azimuth to form the basis of a quantitative 3-D seismic stratigraphy based on well-established geostatistical, clustering, classification, and segmentation analysis methods.

ACKNOWLEDGMENTS

The authors thank their Amoco Business Unit sponsors for both their financial support and technical contributions to our coherency cube analysis effort.

The development of this technology has been a team effort, including careful geologic calibration as well as algorithm design, implementation, and deployment. Team members not listed as coauthors are Norm Haskell, Sue Nissen, Greg Partyka, Kelly Crawford, Mike Nelson, Chris Skirius, Adam Gersztankorn, Ken Kelly, John Lopez, John Duffy, John Groves, Rob Piepul, Joe Burnham, Katrina Coterill, and Janet Cairns.

A patent has been applied for. The patent is Method and apparatus for seismic signal processing and application, PCT International Publication Number WO 97/13166, April 10, 1997.

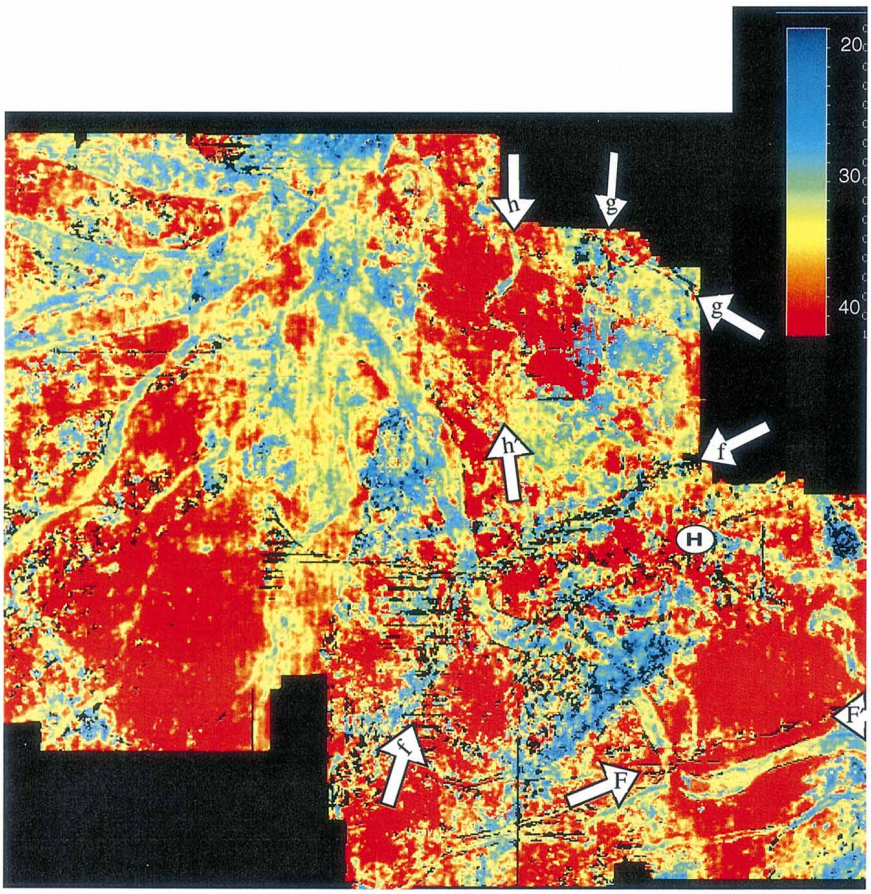

FIG. 21. Reflector response frequency generated using equations (8c), (14c), and (15c) for an eleven-trace analysis window where $a = b = 30$ m. Black corresponds to zones where $c < 0.50$ or where the probability of a reflector is low.

Finally, we thank Margie Meyers, Vicki Wilson, and Julie Youngblood in Amoco's Document Service for preparation of this manuscript.

REFERENCES

Bahorich, M. S., and Bridges, S. R., 1992, The seismic sequence attribute map (SSAM): 42nd Ann. Internat. Mtg., Soc. Expl. Geophys., Expanded Abstracts, 227–230.

Bahorich, M. S., and Farmer, S. L., 1995, 3-D Seismic coherency for faults and stratigraphic features: The Leading Edge, 1053–1058.

——— 1996 U.S. Patent No. 5, 563, 949: Methods of seismic signal processing and exploration.

Bodine, J. H., 1984, Waveform analysis with seismic attributes: Presented at the 54th Ann. Internat. Mtg., Soc. Expl. Geophys.

Bucher, R. H., Marfurt, K. J., and Stanley, T. D., 1988, Method for color mapping geophysical data: U.S. Patent 4 970 699.

Cohen, L., 1993, Instantaneous "anything": Proc. IEEE Int. Conf. Acoust. Speech Signal Proc., **4**, 105–109.

Dalley, R. M., Gevers, E. E. A., Stampli, G. M., Davies, D. J., Gastaldi, C. N., Ruijtenberg, P. R., and Vermeer, G. J. D., 1989, Dip and azimuth displays for 3-D seismic interpretation. First Break, **7**, 86–95.

Foley, J. D., and Van Dam, A., 1981, Fundamentals of interactive graphics: Addison-Wesley Publ. Co.

Gersztenkorn, A., and Marfurt, K. J., 1996, Coherency computations with eigenstructure: Presented at the 58th Internat. Mtg., European Assn. Geoscientists and Engineers, Extended Abstracts, x031.

Haskell, N. L., Nissen, S. E., Lopez, J. A., and Bahorich, M. S., 1995, 3-D seismic coherency and the imaging of sedimentological features in predictive high resolution sequence stratigraphy: Norwegian Petrol. Soc. Conf.

Landa, E., Thore, P., and Reshef, M., 1993, Model-based stack: A method for constructing an accurate zero-offset section for complex overburdens: Geophys. Prosp., **41**, 661–670.

Marfurt, K. J., Sharp, J. A., Scheet, R. M., Ward, J., Cain, G., and Harper, M. G., 1998, Suppression of the acquisition footprint for seismic attribute analysis: Geophysics, **63**, 1024–1035.

Mondt, J. C., 1990, The use of dip and azimuth horizon attributes in 3-D seismic interpretation: SPE 20943, 71–77.

Nissen, S. E., Haskell, N. L., Lopez, J. A., Donlon, T. J., and Bahorich, M. S., 1995, 3-D seismic coherency techniques applied to the identification and delineation of slump features: 65th Ann. Internat. Mtg., Soc. Expl. Geophys., Expanded Abstracts, 1532–1534.

Rijks, E. J. H., and Jauffred, J. E. E. M., 1991, Attribute extraction: An important application in any 3-D interpretation study: The Leading Edge, Sept., 11–19.

Stoffa, P. L., Buhl, P., Diebold, J. B., and Wenzel, F., 1981, Direct mapping of seismic data to the domain of intercept time and ray parameter—A plane wave decomposition: Geophysics, **46**, 255–267.

Taner, M. T., and Koehler, F., 1969, Velocity-spectra digital computer derivation and applications of velocity functions: Geophysics, **39**, 859–881.

Taner, M. T., Koehler, F., and Sheriff, R. E., 1979, Complex seismic trace analysis: Geophysics, **44**, 1041–1063.

Yilmaz, O., and Taner, M. T., 1994, Discrete plane-wave decomposition by least-mean-square-error method: Geophysics, **59**, 973–982.